

Object Wake-up: 3-D Object Reconstruction, Animation, and in-situ Rendering from a Single Image

Xinxin Zuo^{*,†}, Ji Yang^{*}, Sen Wang^{*,†}, Zhenbo Yu[‡], Xinyu Li^{*}, Bingbing Ni^{‡,^}, Minglun Gong[†], Li Cheng^{*}

^{*}University of Alberta [‡]Shanghai Jiao Tong University [^]Huawei Hisilicon [†]University of Guelph

xzuo, jyang7, sen9, xingyu, lcheng5@ualberta.ca

Abstract

Given a picture of a chair, could we extract the 3-D shape of the chair, animate its plausible articulations and motions, and render in-situ in its original image space? The above question prompts us to devise an automated approach to extract and manipulate articulated objects in single images. Comparing with previous efforts on object manipulation, our work goes beyond 2-D manipulation and focuses on articulable objects, thus introduces greater flexibility for possible object deformations. The pipeline of our approach starts by reconstructing and refining a 3-D mesh representation of the object of interest from an input image; its control joints are predicted by exploiting the semantic part segmentation information; the obtained object 3-D mesh is then rigged & animated by non-rigid deformation, and rendered to perform in-situ motions in its original image space. Quantitative evaluations are carried out on 3-D reconstruction from single images, an established task that is related to our pipeline, where our results surpass those of the SOTAs by a noticeable margin. Extensive visual results also demonstrate the applicability of our approach.

1. Introduction

In this paper, we look at the following question: presented with a single input image of an object, say an airplane or a chair, could we make the object come alive and generate interesting videos, such as a chair walking like a dog? The question basically involves the capacity of extracting and manipulating objects in images, which could have many downstream applications in e.g. VR/AR. The problem is akin to photo editing which has already been popular with professional tools such as PhotoShop, but the existing tools are typically confined to objects manipulation purely in 2-D image space, where we can perform basic functions like cut-and-paste and hole-filling, among others.

There have been research efforts [13] that perform 3-D manipulations from a single input image, but they mainly

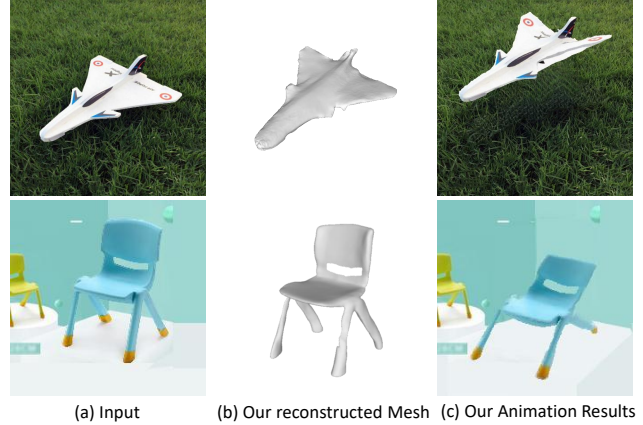


Figure 1. Two exemplar results. Given an input image of airplane or chair, our approach reconstructs its 3-D mesh, and animates its motion in its original image space. The corresponding animations are in supplementary video.

focus on rigid transformations. As to non-rigid deformations, they rely on professional software with intensive user interactions. Our intention is instead to enable flexible manipulation of generic objects in 3-D with motion dynamics akin to humans or animal motions. For example, imagine a chair walks like a dog, or airplane flies like a bird. The objects, as we considered here, are articulable – objects that are capable of being controlled by a skeleton of joints. In a sense, our problem could be considered a generalization of image-based 3-D animation of humans to generic objects we have in our daily life, as long as they could be endowed with a skeleton.

Comparing to the more established topic of human body animation [41], there are nevertheless new challenges to tackle with. One major challenge is, there is no pre-existing parametric shape model for general objects. In human modeling, on the other hand, there are well-developed human template models, such as the SMPL [20] model. Besides, human template naturally comes with its skeletal configuration for 3-D motion control, and the precise skinning weights designed by professionals for shape deformations.

However, such skeletal joints are yet to be specified not to mention the skinning weights in the case of generic objects, which usually have complex and diverse structures.

The observations have motivated us to propose the automated pipeline, as illustrated in Fig. 1. A 3-D object mesh is firstly reconstructed from the input image. The initial mesh is then refined to best fit to its 2-D silhouette and its depth map predicted from a learned monocular depth network. Now, to manipulate this 3-D object, we need to have at hand its skeleton, i.e. a set of control joints in the 3-D mesh. This issue is dealt with by performing semantic segmentation on the 3-D mesh into parts, where the joints are often identified as the intersection point of two consecutive body parts. Instead of calculating the precise skinning weights over the mesh, our animation is then executed by a non-rigid surface deformation strategy. Without loss of generality, four distinct categories of objects are considered in our work, namely chair, table, lamp, and airplane.

We summarize the contributions in this paper:

- An automated pipeline is proposed to reconstruct, animate, and in-situ render 3-D objects from single images. To our knowledge, it is the first attempt to enable in-situ articulation of generic objects in images.
- As an essential component in our pipeline, a novel and effective mesh refinement procedure is developed by aligning to the 2-D silhouette and 3D depth obtained from the input image.
- The semantic segmentation cues are exploited in producing the skeletal joints; non-rigid surface deformation is then engaged for object animation instead of manually fiddling the skinning weights.

Some visually appealing results of our full pipeline are also presented in the experiments that demonstrates the applicability of our approach. Our dataset and code is to be made publicly available upon paper acceptance.

2. Related Work

2.1. Single Image based Object Reconstruction

There have been extensive studies on single image based 3-D object reconstruction with various ways for 3D shape representation, including voxels, octree [30, 35, 40], deep implicit function, mesh and point cloud [6, 17, 29, 23]. Methods based on different representations all have their cons and pros. For example, as a natural extension of 2-D pixels, volumetric representation [7, 38] has been widely used in early efforts due to its simplicity of implementation and compatibility with convolutional neural network. However, these approaches are limited to relatively small voxel grids, due to high memory demand and computational cost. Mesh based representations [10, 19, 39, 14], on the other

hand, take in the initial template mesh and deform it using trained neural nets. It becomes more desirable in real applications, as it is able to model fine shape details, and compatible with various geometry regularizers. It is however still a challenging issue to handle topology change [39, 27]. Deep implicit 3-D representations [28, 4, 18, 37] has recently attracted wide interests in tackling the 3-D reconstruction problem, as a powerful technique in modelling complex shape topologies at arbitrary resolutions. In addition to directly predict the 3-D geometry of an object from RGB images, there are approaches that decompose the problem into sequential steps, which estimate 2.5D information such as depth maps, normal maps. It has the advantage of being more detail preserving than that of directly regressing the 3-D shapes. For example, the recent work of front2back [47] predicts depth map from an input image, and predict the invisible sides with symmetry. However, their output is point cloud, which requires additional non-trivial post-processing steps [2, 12] to deliver the final 3-D mesh.

One common issue of these existing approaches lies in fact that no dedicated effort is made to reconstructed 3-D object mesh that is actually aligned with the input image. This inspires us to explicitly address the alignment issue in our approach.

2.2. Image based Object Animation in 2-D and 3-D

Prior efforts in animating objects from images predominantly focus on 2-D based deformations. A least-square method is considered in [32] to affine transform objects in 2-D. The work of [9] goes beyond linear transformation, by presenting an as-rigid-as-possible 2-D animation of a human character from an image, it is however manual intensive. In [43], 2-D instances of the same visual objects are ordered and grouped to form an instance-based animation of non-rigid motions. Relatively few research activities consider 3-D animations, where they are mostly concerning animals, humans and human-like objects. This line of research benefits significantly from the prior work in establishing the pre-defined skeletal templates and parametric 3-D shape models that are only available for human or animal objects; thus the emphases is on automatic rigging. An early work [1] fits such a pre-defined skeletal template to a 3-D shape, with skinning obtained through heat diffusion. These fittings, unfortunately, tend to fail as the input shapes become less compatible with the skeletal template. More recently, the photo wake-up [41] considers to rig and animate 3-D human shapes from single input images. Xu et al. [44] use deep learning to directly predict joints and skinning weights of the 3-D objects. These efforts however heavily hinge on availability of large-scale well-annotated datasets of skeletal joints and skinning weights. On the other hand, few efforts including [13] consider 3D manipulations of generic objects from images, meanwhile

they mainly focus on rigid transformations. Our work could be regarded as an extension of automated image-based human shape reconstruction & rigging to articulate & animate generic lifeless objects.

3. Our Approach

An overview of our pipeline is provided in Fig. 2.

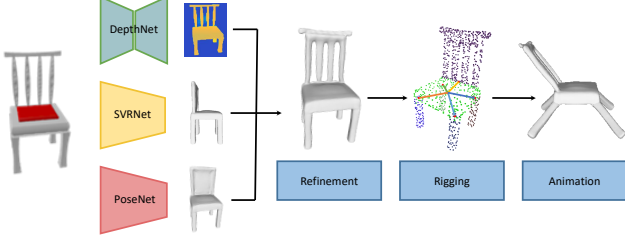


Figure 2. An overview of our pipeline. From an input image, the trio of DepthNet (Sec.3.1), SVRNet (Sec.3.1), and PoseNet (Sec.3.1) are engaged to reconstruct the 3-D mesh of the object that conforms to its estimated 3-D depth and 2-D silhouette constraints. Briefly, the SVRNet provides an initial 3-D mesh based on deep implicit function [22]; DepthNet provides monocular depth estimation using a Res18-UNet structure; PoseNet is to align the 3D mesh to the camera coordinate system. The obtained 3-D object mesh is then refined (as in Sec.3.2), rigged & animated (as in Sec.3.3) in the original image space. The occluded image region is in-painted to provide a complete scene background.

3.1. Single Image 3-D Object Reconstruction

Our reconstruction framework contains three branches: SVRNet to provide an initial 3-D mesh based on the deep implicit function of [22], DepthNet for depth map estimation, and PoseNet to map to the camera coordinate system. The three branches are combined in the mesh refinement process to deliver final 3-D mesh consistent with information obtained from the input image. For the initial model prediction branch (SVRNet), we exploit a current state-of-the-art method [22] which could predict the overall shape of the object on single image 3-D reconstruction.

DepthNet for Depth Estimation. For depth estimation, we adopt the Res18-UNet structure to predict both the depth and the normal map from a given input image. We define the loss function as the sum of $L1$ loss on the predicted depth as well as $L1$ loss on the predicted normal map together with depth balanced Euclidean (DBE) loss [16] for better convergence.

PoseNet for Rigid Pose Estimation. Given a single image as input, the aim is to regress the 6 DoF camera parameters of rotation and translation to transform the initial 3-D model to the camera space. Here we consider a simple yet effective procedure similar to [42]. Instead of directly predicting the rotation matrix which is difficult for a neural network to train and converge, we employ the 6-D rotation

representation. The network structure follows a common "encoder-regressor" strategy: the ResNet-18 [8] is used as the backbone encoder to generate features, followed by a regressor that predicts the 6-D rotation & translation. The 3-D distance loss, L_{3D} , is defined as the mean squared error between the transformed point cloud and the ground truth point cloud in the camera space,

$$L_{3D} = \|\mathbf{p}_{GT} - (\mathbf{R}\mathbf{p}_w + \mathbf{t})\|_2^2, \quad (1)$$

where \mathbf{R} and \mathbf{t} denote the predicted rotation and translation respectively. $\mathbf{p}_w \in \mathbb{R}^{N \times 3}$ is the point cloud in the canonical space and N is the number of points. \mathbf{p}_{GT} indicates the corresponding ground truth point cloud of \mathbf{p}_w in camera space.

In addition, a 2-D soft IoU loss, L_{2D} , is introduced by differentiable rendering to project the transformed mesh to the image plane, and by computing 2-D IoU loss for the projected mask and the object mask of the input image,

$$L_{2D} = \|\mathbf{I}_m - f_{DR}(\mathbf{R}\mathbf{p}_w + \mathbf{t})\|_2^2, \quad (2)$$

where f_{DR} indicates the differentiable rendering process that projects a mesh to an image, and I_m is the object mask in the input image.

The initial pose from PoseNet is then refined by a per-instance optimization procedure by minimizing the above 2-D and the 3-D losses: the 2-D loss is evaluated between the ground-truth mask and the rendered mask; the 3-D loss is the distance between the point and triangle mesh. 3-D point cloud is obtained by back projecting the regressed depth map and minimize its distance to the predicted 3-D mesh from SVRNet.

3.2. Mesh Refinement

With the predicted camera pose, our 3-D mesh obtained from SVRNet can be transformed to the camera space. As illustrated in Fig. 3(a), a noticeable misalignment is revealed, when the rendered mask from our 3-D mesh is overlay to the ground-truth mask in the input image. This leads to a mesh refinement process with the following three steps of deform, remove, and inpaint.

Deform. The goal is to displace the vertices of the current mesh to minimize the misalignment between the rendered mask and the ground-truth mask in the input image. This is achieved by examine the 3-D displacement, ΔX , of each mesh vertex, as minimizing the following objective function,

$$E(\Delta X) = \sum_i \|f_{DR}(X_i + \Delta X_i) - C_{\phi(i)}\| + \lambda_{ds} \sum_{(i,j) \in \mathcal{N}} \|((X_i + \Delta X_i) - (X_j + \Delta X_j)) - R_i(X_i - X_j)\|. \quad (3)$$

Here X denotes each mesh vertex and ΔX is its displacements; \mathcal{N} is the set of vertex in 1-ring neighbor. C de-

notes the object boundary from the image; $\phi(i)$ is the correspondence between the mesh and the object in the input image. We get the correspondence association by projecting the current mesh onto the image to obtain the rendered object boundary, and compute the matches from the rendered boundary to the ground-truth boundary. We use the predicted depth map d^s from DepthNet as guidance. Specifically, we compute the gradient map for both the rendered depth d^s and predicted depth map d^r . For each pixel on the rendered boundary, we search for the nearest corresponding pixel in 3-D space on the ground-truth boundary having consistent gradient direction on the two depth maps (d^s and d^r).

The first term thus penalizes the distance between the rendered silhouette and the ground-truth silhouette in input image. The second term is to enforce an as-rigid-as-possible constraint to improve local smoothness of the deformed mesh. It is assumed that the neighboring vertices after applying the displacement should have nearly the same rotations R_i as on the original mesh. λ_{ds} denotes the weight for the smooth deformation constraint. Finally, the above objective function of Eq. (3) is solved by iteratively updating the correspondence association and displacement computation. Note the local rotation R_i is set to an identity matrix and should also be updated iteratively. More details could be found in [33].

Remove. The above operation deforms the current 3-D mesh to better match the image object. However, deformation alone can not change the mesh topology, as shown in the first row of Fig. 3. This leads to the introduction of the remove step to eliminate the faces violating the following constraints: 1) the projected faces should always stay inside the object silhouettes; 2) the projected depth should not be smaller than the corresponding values in the predicted depth map. A predefined threshold, thres_d , is used to compensate for the imperfect depth prediction. Instead of directly removing the faces which will result in an open boundary over the mesh, we adopt a strategy similar to space carving [15]. We embed the mesh into the volumetric representation and re-compute the sign distance function of the voxel that violates the above constraints to lie outside of the surface. The output mesh can be extracted from the updated sign distance function via Marching Cubes[21].

Inpaint. As suggested in the second row of Fig. 3, it is rather difficult in the deform stage to generate the detailed structure completely missing in the current mesh. This gives rise to the inpainting step. In detail, we project the current mesh model into the 2-D image space to get the corresponding depth map d^r . Then the pixels which lie inside of the silhouettes but do not have rendered depth value are flagged as to be inpainted, denoted as \mathcal{O} . We take advantage of the predicted depth map d^s from our DepthNet as guidance. Instead of directly using the depth value, the gradient

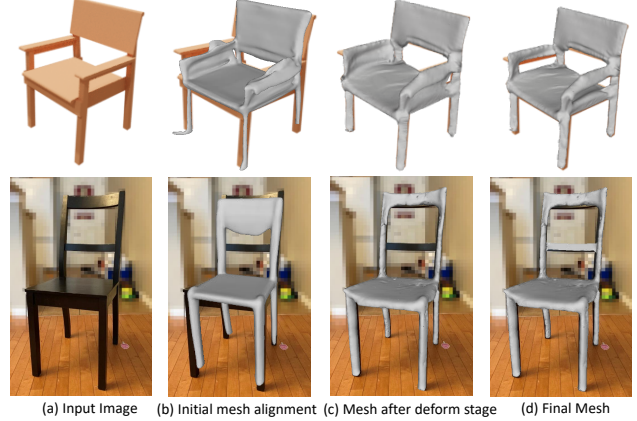


Figure 3. Exemplar results of mesh refinement. (a) input images. (b) the initial mesh from SVRNet. (c) after deform stage (d) final result.

of the predicted depth map is used to constrain the inpainting. Mathematically, the inpainted depth map d is obtained by minimizing the following objective function,

$$E(d) = \sum_{p \in \mathcal{B}} \|d_p - d_p^r\| + \sum_{p \in \mathcal{O}} \|\delta d_p - \delta d_p^s\|. \quad (4)$$

Here δd is the gradient of the depth map; \mathcal{B} denotes the set of the neighboring pixels of the inpainted pixels which have rendered depth values. The first term enforces the boundary constraint for the inpainting to maintain smooth transition and connectivity between the current mesh and the inpainted mesh. The second term maintains consistency between inpainted depth and predicted depth d^s in the gradient domain. Finally, the inpainted mesh from the depth map is merged with the current mesh to produce a 3-D mesh matching up to the image object, as exemplified in the second row of Fig. 3.

3.3. Automatic Rigging and Animation

The skeletal joints and rigging are to be settled first prior to animation. Prior efforts [45, 44] regressing the joints and skinning weights with deep learning unfortunately relying on large & well-annotated datasets of humans or animals, which are not suitable here. Instead we propose to exploit semantic segmentation to infer the control joints.

The semantic part-based segmentation uses a state-of-the-art method [36], trained on the ShapeNetSem dataset [31] and PartNet dataset [24]. This is followed by a conditional random field-based smoothing optimization [46] to filter out redundant noise.

Joints Prediction and Automatic Rigging via Semantic Segmentation. The semantic part-based segmentation provides a valuable and meaningful decomposition of the 3-D shape into local parts, which facilitates the prediction of skeletal joints by the following steps:

First, we compute the connecting boundary between neighboring parts. Following the predefined semantic labels, we find every two possible neighboring parts. Basically, for every two candidate neighboring parts, we use k-nearest search to find the corresponding vertices between two parts. If the distance between corresponding vertices is below a predefined threshold thres_n , it is taken as the connecting boundary vertices. Otherwise, if the minimum distance between the two parts is above the threshold, these two parts are regarded as non-neighboring parts. Given those connecting boundaries (as shown in Fig. 4(c)), we compute the control joints as the mean of those connecting vertices. Optionally, we could also compute the center for every segmented part as control joints to increase animation flexibility.

We assign semantic labels to the detected control joints according to the semantic part information. Starting from this, we define the protocols to build up the kinematic chain for those joints. For example, as shown in Fig. 4(d), for the chair model, we set the root joint as the center of the chair seat. Starting from this root joint, we have the connecting joint between the chair seat and chair leg as the children node. In this way, we introduce the flexibility of manipulating the chair seat, back and its four legs independently.

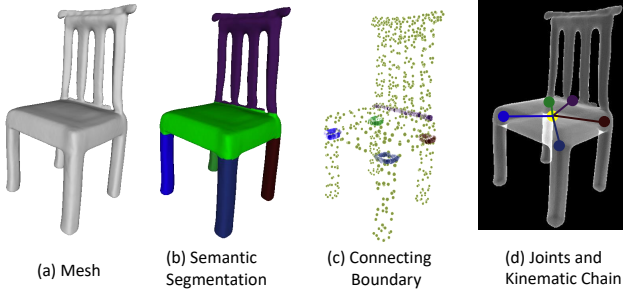


Figure 4. Joints extraction process.

Finally, to implement animation we still need to compute the skinning weights to bind each vertex to the joints. A basic assumption in previous skin attachment methods is that the vertex will be largely controlled by the nearest joint measured in Euclidean distance. However, exploiting Euclidean distance might not be ideal for general objects which will introduce improper deformation in some cases. For example, the vertices on the airplane wings are assumed to be dominated by one control joint. However, as shown in Fig. 5(c) where the color indicates the control weight of the vertices with respect to the joints, the estimated skinning weights using Euclidean distance indicate that deformation of the vertices in the same wing are dominated by two different joints. To get meaningful animation, we choose to assign the skinning weights by utilizing the semantic part segmentation. For each object category, we define a protocol to assign the skinning weights. For example, we set the

dominate joints for the vertices labeled as airplane wings to be the connecting joints between the wings and the body. The details about the predefined protocol are described in supplementary.

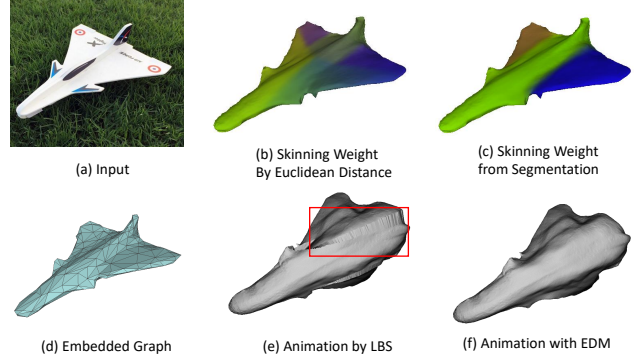


Figure 5. Comparison on computed skinning weights and animation. (a) input image. (b) the computed skinning weight, measured by Euclidean distance. (c) our computed skinning weight where the airplane wing is dominated by one joint instead of two different control joints. (d) the embedded graph built for deformation. (e) the deformed mesh using linear blend skinning. (f) the deformed mesh by our proposed strategy.

Animation by Deformation. Given the computed control joints and corresponding skinning weights for each vertex, we can conduct the animation afterward. The current issue is that the computed skinning weights are not precisely correct which will introduce artifacts to the deformed mesh especially around the joints, as shown in Fig. 3(d). To deal with this problem, instead of developing sophisticated skinning weights computation strategies, we propose to utilize the non-rigid surface deformation technique to realize the animation. Specifically, we use the embedded deformation (EDM) [34]. For the deformation model, a set of graph nodes (g_1, g_2, \dots, g_K) are uniformly sampled throughout the mesh, and for each node g_i , it has an affine transformation specified by a 3×3 matrix A_i and a 3×1 translation vector t_i . For each vertex v on the mesh it is controlled and deformed by its K nearest graph nodes with a set of weights:

$$\Phi(v) = \sum_{i=1}^K w_i(v) [A_i(v - g_i) + g_i + t_i] \quad (5)$$

We build a graph for the current mesh model to be animated and estimate the deformation parameters $A_1 \sim A_l$ (denoted as \mathcal{A}) and $t_1 \sim t_l$ (denoted as \mathcal{T}) by minimizing the following objective function:

$$E(\mathcal{A}, \mathcal{T}) = E_{ctrl}(\mathcal{A}, \mathcal{T}) + \lambda_{reg} E_{reg}(\mathcal{A}) + \lambda_s E_s(\mathcal{A}, \mathcal{T}) \quad (6)$$

First of all, E_{ctrl} enforces the vertices after deformation should be close to the deformed vertices obtained from the

above linear blend skinning (LBS) [11] deformation. We set the control vertices as the vertices (denoted as V_{ctrl}) away from the segmentation boundary.

$$E_{ctrl}(\mathcal{A}, \mathcal{T}) = \sum_{v \in V_{ctrl}} \|\Phi(v) - f_v(\theta, \Omega)\|, \quad (7)$$

$$f_v(\theta, \Omega) = \left(\sum_{j=1}^m \Omega_{v,j} T_j(\theta) \right) v \quad (8)$$

where $\Omega_{v,j}$ is the skinning weight matrix and $T(\theta)$ is the transformation matrix of control joints which is related to the rotation angle of the control joints. m is the number of control joints.

The term E_{reg} serves as the as-rigid-as-possible term preventing arbitrary surface deformation.

$$E_{reg}(\mathcal{A}) = \sum_{i=1}^l \|\mathbf{A}_i \mathbf{A}_i^T - \mathbf{I}\|_2^2 \quad (9)$$

The smoothness term E_s ensures smooth deformation of neighboring graph nodes.

$$E_s(\mathcal{A}, \mathcal{T}) = \sum_{(i,j) \in \mu} \|\mathbf{A}_i(g_j - g_i) + g_i + \mathbf{t}_i - (g_j + \mathbf{t}_j)\|_2^2 \quad (10)$$

We minimize the energy function via the iterative Gauss-Newton algorithm to get the affine matrix and translation vector controlled by which we will get the deformed mesh. As shown in Fig. 3(f), with the as-rigid-as-possible deformation strategy, we can obtain the animated mesh model which has a more natural and smooth transition around part boundaries.

4. Experiments

Implementation Details. The object is masked out with image segmentation method under some user interaction. We exploit the image inpainting approach proposed in [48] to generate the background image. To obtain the texture map of the reconstructed 3-D model, we apply mirror texture for the invisible part. In the semantic part segmentation, the four legs of a chair are all labeled as Chair Leg. So we further perform clustering on the point cloud labeled as Chair Leg to segment each chair leg. We perform the same processing to Table and Airplane models. The parameter λ_{ds} is set to be 5.0, λ_s is 10, λ_{reg} is 100, thres_d is 0.05, and thres_n is 0.02.

Datasets. Both rigid camera pose and 3-D object reconstruction are trained on the ShapeNetCore dataset [3] following the its official training/testing split. Here we focus on four categories: chair, table, lamp, airplane. For rigid pose and 3-D object reconstruction, the rendered train/test images from [5] are used. For depth estimation, 256×256

depth and color images of objects in the ShapeNetCore are rendered. Except for the camera intrinsic parameters, the same configurations in [5] are used in the rendering process.

Rigid Pose Estimation. Direct estimation of the error on the transformation matrix is meaningless to our framework. Instead, we evaluate the predicted camera pose using the mean distance d_{3D} between the point cloud transformed by the ground truth and by the predicted camera pose. Also, the 2-D IoU error is evaluated between the transformed mesh after projection and the groundtruth mask.

We compare our camera pose estimation with DISN [42] which we are dealing with similar problems. For a fair comparison, we only use the quantitative result before the per-instance optimization in our proposed pipeline. Quantitative results are reported in Table 1. By introducing a differentiable rendering based loss, we are able to outperform [42] on both the 3-D mean distance d_{3D} and the 2-D IoU after projection.

	DISN [42]	Ours
d_{3D}	0.047	0.039
IoU	0.778	0.815

Table 1. Quantitative results of camera pose estimation.

Evaluation on Reconstruction. We compare with several state-of-the-art methods on single image object reconstruction. We directly use the pre-trained model released by the user. For evaluation metrics, we use the Chamfer Distance (CD) between the ground truth and reconstructed meshes by evenly sampling 10k points on the two meshes. For a fair comparison, we apply scaled rigid ICP [25] between the predicted and the groundtruth model to cancel out the effect of global transformation when computing the Chamfer distance. Also, we evaluate the projection IoU which indicates how well the reconstructed mesh is aligned with the input image in the image space. We show the evaluation results in Tab. 2, from which we can see that our method has outperformed the comparison methods in a big margin on both Chamfer Distance and projection IoU.

In Fig. 6, we show the qualitative evaluation on the ShapeNet dataset. As demonstrated in the figure, all compared methods could predict the overall shape of the object, but it is difficult to restore the structure details of the model. For example, both the OccNet [22] and DVR method [26] fail to recover structure on the chair back. And the compared methods all fail to reconstruct the lamp body which is a quite thin structure. In contrast, our method is able to capture complex structure details and preserves most of the details even for the very thin lamp body as shown in the second row of Fig. 6.

Animation Results. In this section, we conduct the animation for objects from real images. In Fig. 7, we demonstrate the manipulation of an airplane. The airplane is re-

method	Chamfer Distance					Projection IoU				
	Chair	Table	Lamp	Airplane	ave.	Chair	Table	Lamp	Airplane	ave.
OccNet [22]	0.9705	1.0731	2.9381	0.8933	1.1910	0.7919	0.8457	0.6702	0.6939	0.7813
DISN [42]	1.2188	2.6651	4.7426	1.3814	2.2029	0.7861	0.8366	0.6479	0.7060	0.7757
DVR [26]	1.0890	1.7392	2.7705	0.8451	1.4816	0.7847	0.8315	0.6555	0.6823	0.7697
Ours	0.7369	0.8683	2.3301	0.6177	0.9721	0.8658	0.8941	0.7406	0.7795	0.8470

Table 2. Image-based 3-D mesh reconstruction on ShapeNet benchmark. Metrics are Chamfer Distance ($\times 0.001$, the smaller the better) and Projection IoU (the larger the better). Best results are in **bold face**.

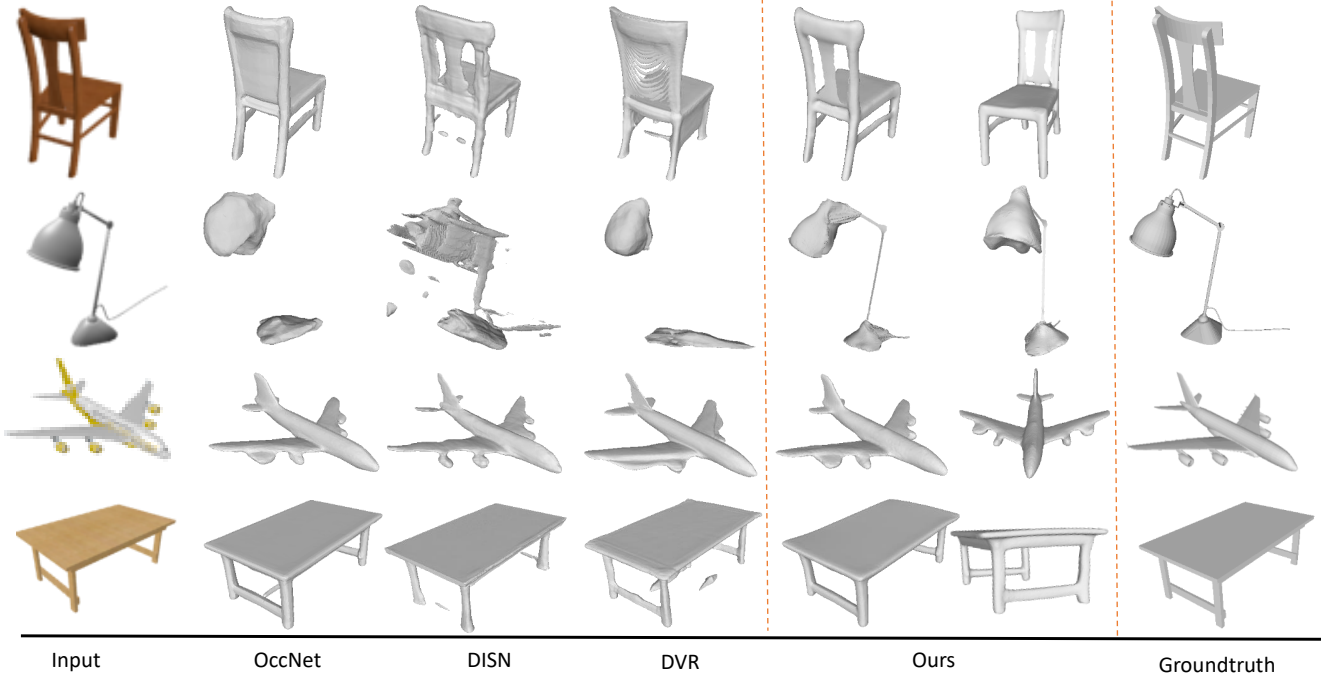


Figure 6. Visual results of image-based 3-D mesh reconstruction on ShapeNet. The input image is shown to the left, the rest columns show the results of the comparison methods.

constructed with our proposed approach and it is segmented into three semantic parts (body, left/right wing). We detect three control joints and build the kinematic chain. The joint controlling the body is set as the root joint and the other two joints are used to control the two wings respectively. By adjusting the angle of the two wings as well as the global transformation, we achieve the final animation effect with the airplane flying over the floor as shown in Fig. 7(b). Similarly, in Fig. 8 we also demonstrate another animation result on a chair. The reconstructed chair model is initially segmented into four legs, chair seat and chair back. To increase animation flexibility, we further detect the center point of each chair leg, after which we can bend the chair legs and generate the animated results as shown in Fig. 8.

In addition, we show that, in Fig. 9 and Fig. 10, we can also animate the objects as driven by other source motion. As shown in Fig. 9, the reconstructed Lamp model is initially segmented into three parts (body, base, head) and we further detect the center point of the lamp body, after which

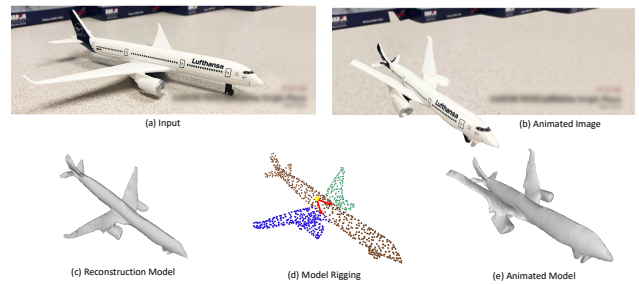


Figure 7. an airplane example. (a) input image. (c) our reconstructed 3-D mesh. (d) semantic segmentation and the predicted skeletal joints. (e) our 3-D animated mesh. (b) our rendered image.

we could map the joints on the human legs to the lamp and generate the animated results with the lamp squatting down like the human. The animated lamp is further scaled and translated, and finally rendered back onto the original image as shown in Fig. 9(c). In Fig. 10, the reconstructed Ta-

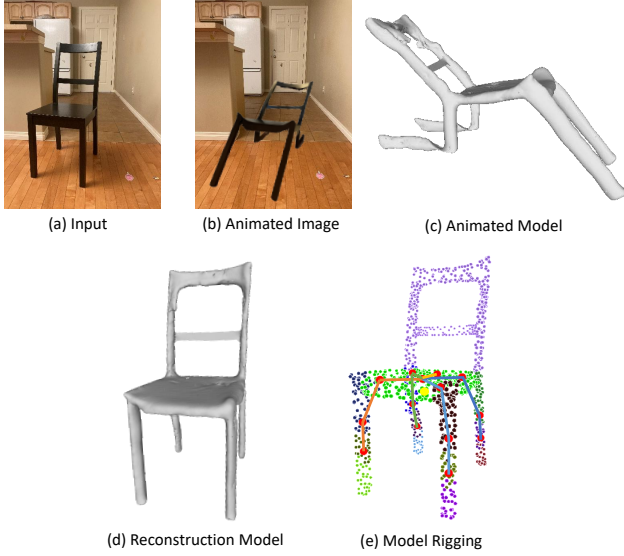


Figure 8. A chair example. (a) input image. (d) our reconstructed 3-D mesh. (e) semantic segmentation and the predicted skeletal joints. (c) our 3-D animated mesh. (b) our rendered image.

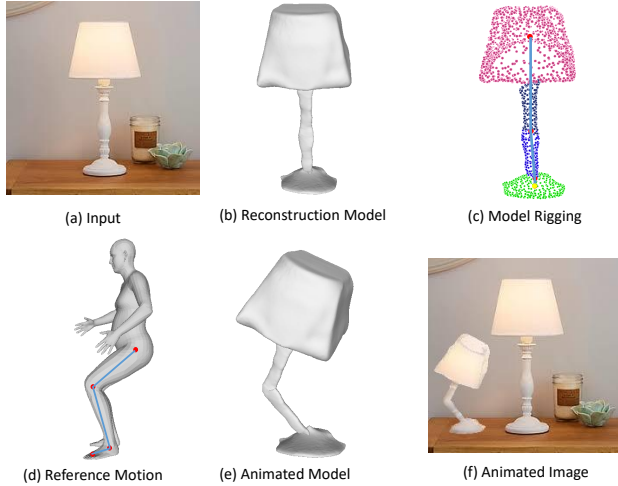


Figure 9. A lamp example. (a) input image. (b) our reconstructed 3-D mesh. (c) semantic segmentation and the predicted skeletal joints. (e) the animated 3-D mesh driven by the human subject of (d). (f) our rendered image.

ble model is animated as driven by a motion from a dog. To have proper joint mapping, we first compute center joint for each table leg to decompose the chair into two parts. And then we further decompose the low part of the table leg and add the center joint as another control joint. Afterwards, we could map the joints on the leg of the dog to the three joints over the table legs. We show the animation results on a walking pose (the second row in Fig. 10) as well as a jumping pose (the third row in Fig. 10).

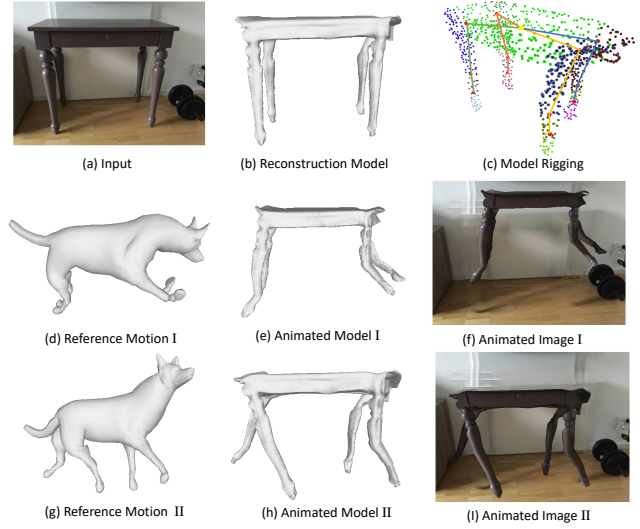


Figure 10. A table result. (a) input image. (b) our reconstructed 3-D mesh. (c) semantic segmentation and the predicted skeletal joints. (e) and (h) the animated 3-D meshes driven by the dog of (d) and (g), respectively. (f) and (i) our rendered images.

5. Conclusion

We consider an interesting task of waking-up 3-D object from a single input image. Our approach is capable of reconstructing the 3-D object mesh, animating the object with plausible articulations, and render back in the original image space. Quantitative and qualitative experiments demonstrate the applicability of our work when unseen real-world images are presented at test time. For future work, we plan to explore its applicability in working with diverse images containing objects from a broad range of categories.

References

- [1] Ilya Baran and Jovan Popović. Automatic rigging and animation of 3d characters. *ACM Transactions on graphics(TOG)*, 26(3):72, 2007. 2
- [2] Fatih Calakli and Gabriel Taubin. Ssd: Smooth signed distance surface reconstruction. *Computer Graphics Forum*, 30(7):1993–2002, 2011. 2
- [3] Angel X Chang, Thomas Funkhouser, Leonidas Guibas, Pat Hanrahan, Qixing Huang, Zimo Li, Silvio Savarese, Manolis Savva, Shuran Song, Hao Su, et al. Shapenet: An information-rich 3d model repository. *arXiv preprint arXiv:1512.03012*, 2015. 6
- [4] Zhiqin Chen and Hao Zhang. Learning implicit fields for generative shape modeling. In *Proceedings of the IEEE/CVF Conference on Computer Vision and Pattern Recognition*, pages 5939–5948, 2019. 2
- [5] Christopher B Choy, Danfei Xu, JunYoung Gwak, Kevin Chen, and Silvio Savarese. 3d-r2n2: A unified approach for single and multi-view 3d object reconstruction. In *European conference on computer vision*, pages 628–644. Springer, 2016. 6

- [6] Haoqiang Fan, Hao Su, and Leonidas J Guibas. A point set generation network for 3d object reconstruction from a single image. In *Proceedings of the IEEE conference on computer vision and pattern recognition*, pages 605–613, 2017. 2
- [7] Georgia Gkioxari, Jitendra Malik, and Justin Johnson. Mesh r-cnn. In *Proceedings of the IEEE/CVF International Conference on Computer Vision*, pages 9785–9795, 2019. 2
- [8] Kaiming He, Xiangyu Zhang, Shaoqing Ren, and Jian Sun. Deep residual learning for image recognition. In *Proceedings of the IEEE conference on computer vision and pattern recognition*, pages 770–778, 2016. 3
- [9] Alexander Hornung, Ellen Dekkers, and Leif Kobbelt. Character animation from 2d pictures and 3d motion data. *ACM Transactions on Graphics(TOG)*, 26(1):1, 2007. 2
- [10] Hiroharu Kato, Yoshitaka Ushiku, and Tatsuya Harada. Neural 3d mesh renderer. In *Proceedings of the IEEE conference on computer vision and pattern recognition*, pages 3907–3916, 2018. 2
- [11] Ladislav Kavan, Steven Collins, Jiří Žára, and Carol O’Sullivan. Skinning with dual quaternions. In *Proceedings of the 2007 symposium on Interactive 3D graphics and games*, pages 39–46, 2007. 6
- [12] Michael Kazhdan and Hugues Hoppe. Screened poisson surface reconstruction. *ACM Transactions on Graphics (ToG)*, 32(3):1–13, 2013. 2
- [13] Natasha Kholgade, Tomas Simon, Alexei Efros, and Yaser Sheikh. 3d object manipulation in a single photograph using stock 3d models. *ACM Transactions on Graphics(TOG)*, 33(4):1–12, 2014. 1, 2
- [14] Dominik Kulon, Riza Alp Guler, Iasonas Kokkinos, Michael M Bronstein, and Stefanos Zafeiriou. Weakly-supervised mesh-convolutional hand reconstruction in the wild. In *Proceedings of the IEEE/CVF Conference on Computer Vision and Pattern Recognition*, pages 4990–5000, 2020. 2
- [15] Kiriakos N Kutulakos and Steven M Seitz. A theory of shape by space carving. *International journal of computer vision*, 38(3):199–218, 2000. 4
- [16] Jae-Han Lee, Minhyeok Heo, Kyung-Rae Kim, and Chang-Su Kim. Single-image depth estimation based on fourier domain analysis. In *IEEE Conference on Computer Vision and Pattern Recognition*, pages 330–339, 2018. 3
- [17] Chen-Hsuan Lin, Chen Kong, and Simon Lucey. Learning efficient point cloud generation for dense 3d object reconstruction. In *proceedings of the AAAI Conference on Artificial Intelligence*, volume 32, 2018. 2
- [18] Chen-Hsuan Lin, Chaoyang Wang, and Simon Lucey. Sdfsrn: Learning signed distance 3d object reconstruction from static images. In *Advances in Neural Information Processing Systems*, 2020. 2
- [19] Shichen Liu, Tianye Li, Weikai Chen, and Hao Li. Soft rasterizer: A differentiable renderer for image-based 3d reasoning. In *IEEE/CVF International Conference on Computer Vision*, pages 7708–7717, 2019. 2
- [20] Matthew Loper, Naureen Mahmood, Javier Romero, Gerard Pons-Moll, and Michael J. Black. SMPL: A skinned multi-person linear model. *ACM Transactions on Graphics(TOG)*, 34(6):248, 2015. 1
- [21] William E Lorensen and Harvey E Cline. Marching cubes: A high resolution 3d surface construction algorithm. *ACM siggraph computer graphics*, 21(4):163–169, 1987. 4
- [22] Lars Mescheder, Michael Oechsle, Michael Niemeyer, Sebastian Nowozin, and Andreas Geiger. Occupancy networks: Learning 3d reconstruction in function space. In *Proceedings of the IEEE/CVF Conference on Computer Vision and Pattern Recognition*, pages 4460–4470, 2019. 3, 6, 7
- [23] Zhenxing Mi, Yiming Luo, and Wenbing Tao. Ssrnet: scalable 3d surface reconstruction network. In *Proceedings of the IEEE/CVF Conference on Computer Vision and Pattern Recognition*, pages 970–979, 2020. 2
- [24] Kaichun Mo, Shilin Zhu, Angel X Chang, Li Yi, Subarna Tripathi, Leonidas J Guibas, and Hao Su. Partnet: A large-scale benchmark for fine-grained and hierarchical part-level 3d object understanding. In *IEEE/CVF Conference on Computer Vision and Pattern Recognition*, pages 909–918, 2019. 4
- [25] Andriy Myronenko and Xubo Song. Point set registration: Coherent point drift. *IEEE transactions on pattern analysis and machine intelligence*, 32(12):2262–2275, 2010. 6
- [26] Michael Niemeyer, Lars Mescheder, Michael Oechsle, and Andreas Geiger. Differentiable volumetric rendering: Learning implicit 3d representations without 3d supervision. In *Proceedings of the IEEE/CVF Conference on Computer Vision and Pattern Recognition*, pages 3504–3515, 2020. 6, 7
- [27] Junyi Pan, Xiaoguang Han, Weikai Chen, Jiapeng Tang, and Kui Jia. Deep mesh reconstruction from single rgb images via topology modification networks. In *Proceedings of the IEEE International Conference on Computer Vision*, pages 9964–9973, 2019. 2
- [28] Jeong Joon Park, Peter Florence, Julian Straub, Richard Newcombe, and Steven Lovegrove. DeepSDF: Learning continuous signed distance functions for shape representation. In *Proceedings of the IEEE/CVF Conference on Computer Vision and Pattern Recognition*, pages 165–174, 2019. 2
- [29] Charles R Qi, Li Yi, Hao Su, and Leonidas J Guibas. Pointnet++: Deep hierarchical feature learning on point sets in a metric space. In *Advances in Neural Information Processing Systems*, 2017. 2
- [30] Gernot Riegler, Ali Osman Ulusoy, and Andreas Geiger. Octnet: Learning deep 3d representations at high resolutions. In *Proceedings of the IEEE conference on computer vision and pattern recognition*, pages 3577–3586, 2017. 2
- [31] Manolis Savva, Angel X. Chang, and Pat Hanrahan. Semantically-enriched 3d models for common-sense knowledge. 2015. 4
- [32] Scott Schaefer, Travis McPhail, and Joe Warren. Image deformation using moving least squares. *ACM Transactions on Graphics(TOG)*, 25(3):533–540, 2006. 2
- [33] Olga Sorkine and Marc Alexa. As-rigid-as-possible surface modeling. In *Symposium on Geometry processing*, volume 4, pages 109–116, 2007. 4
- [34] Robert W Sumner, Johannes Schmid, and Mark Pauly. Embedded deformation for shape manipulation. *ACM Transactions on Graphics(TOG)*, 26(3):80, 2007. 5

- [35] Maxim Tatarchenko, Alexey Dosovitskiy, and Thomas Brox. Octree generating networks: Efficient convolutional architectures for high-resolution 3d outputs. In *Proceedings of the IEEE International Conference on Computer Vision*, pages 2088–2096, 2017. 2
- [36] Hugues Thomas, Charles R Qi, Jean-Emmanuel Deschaud, Beatriz Marcotequi, François Goulette, and Leonidas J Guibas. Kpconv: Flexible and deformable convolution for point clouds. In *Proceedings of the IEEE/CVF International Conference on Computer Vision*, pages 6411–6420, 2019. 4
- [37] Edgar Tretschk, Ayush Tewari, Vladislav Golyanik, Michael Zollhöfer, Carsten Stoll, and Christian Theobalt. Patchnets: Patch-based generalizable deep implicit 3d shape representations. In *European Conference on Computer Vision*, pages 293–309. Springer, 2020. 2
- [38] Shubham Tulsiani, Alexei A Efros, and Jitendra Malik. Multi-view consistency as supervisory signal for learning shape and pose prediction. In *Proceedings of the IEEE conference on computer vision and pattern recognition*, pages 2897–2905, 2018. 2
- [39] Nanyang Wang, Yinda Zhang, Zhuwen Li, Yanwei Fu, Wei Liu, and Yu-Gang Jiang. Pixel2mesh: Generating 3d mesh models from single rgb images. In *European Conference on Computer Vision (ECCV)*, pages 52–67, 2018. 2
- [40] Peng-Shuai Wang, Yang Liu, and Xin Tong. Deep octree-based cnns with output-guided skip connections for 3d shape and scene completion. In *Proceedings of the IEEE/CVF Conference on Computer Vision and Pattern Recognition Workshops*, pages 266–267, 2020. 2
- [41] Chung-Yi Weng, Brian Curless, and Ira Kemelmacher-Shlizerman. Photo wake-up: 3d character animation from a single photo. In *IEEE/CVF Conference on Computer Vision and Pattern Recognition*, pages 5908–5917, 2019. 1, 2
- [42] Qiangeng Xu, Weiyue Wang, Duygu Ceylan, Radomir Mech, and Ulrich Neumann. Disn: Deep implicit surface network for high-quality single-view 3d reconstruction. In *Advances in Neural Information Processing Systems*, pages 492–502, 2019. 3, 6, 7
- [43] Xuemiao Xu, Liang Wan, Xiaopei Liu, Tien-Tsin Wong, Liansheng Wang, and Chi-Sing Leung. Animating animal motion from still. In *ACM SIGGRAPH Asia*, pages 1–8. 2008. 2
- [44] Zhan Xu, Yang Zhou, Evangelos Kalogerakis, Chris Landreth, and Karan Singh. Rignet: Neural rigging for articulated characters. *ACM Transactions on Graphics(TOG)*, 39(58), 2020. 2, 4
- [45] Zhan Xu, Yang Zhou, Evangelos Kalogerakis, and Karan Singh. Predicting animation skeletons for 3d articulated models via volumetric nets. In *2019 International Conference on 3D Vision (3DV)*, pages 298–307, 2019. 4
- [46] Jian Yao, Sanja Fidler, and Raquel Urtasun. Describing the scene as a whole: Joint object detection, scene classification and semantic segmentation. In *Proceedings of the IEEE Conference on Computer Vision and Pattern Recognition*, pages 702–709, 2012. 4
- [47] Yuan Yao, Nico Schertler, Enrique Rosales, Helge Rhodin, Leonid Sigal, and Alla Sheffer. Front2back: Single view 3d shape reconstruction via front to back prediction. In *IEEE/CVF Conference on Computer Vision and Pattern Recognition*, pages 531–540, 2020. 2
- [48] Zili Yi, Qiang Tang, Shekoofeh Azizi, Daesik Jang, and Zhan Xu. Contextual residual aggregation for ultra high-resolution image inpainting. In *IEEE/CVF Conference on Computer Vision and Pattern Recognition*, pages 7508–7517, 2020. 6